

# Recent advances in colloidal gold nanobeacons for molecular photoacoustic imaging<sup>†</sup>

Dipanjan Pan<sup>a\*</sup>, Manojit Pramanik<sup>b</sup>, Samuel A. Wickline<sup>a,b</sup>,  
Lihong V. Wang<sup>b</sup> and Gregory M. Lanza<sup>a,b</sup>

Photoacoustic imaging (PAI) represents a hybrid, nonionizing modality, which has been of particular interest because of its satisfactory spatial resolution and high soft tissue contrast. PAI has the potential to provide both functional and molecular imaging *in vivo* since optical absorption is sensitive to physiological parameters. In this review we summarize our effort to advance molecular PAI with colloidal gold nanobeacons (GNB). GNB represents a robust nanoparticle platform that entraps multiple copies of tiny gold nanoparticles (2–4 nm) within a larger colloidal particle encapsulated by biocompatible synthetic or natural amphiphiles. The utilization of numerous small gold particles greatly amplifies the signal without exceeding the renal elimination threshold size. With fibrin-targeted GNB, the robust detection of microthrombus formed over a ruptured atherosclerotic plaque has been achieved, which offers an important opportunity to recognize patients with moderate lumen stenosis but high risk of stroke. With the use of second-generation smaller GNBs, the potential to improve sentinel lymph node assessment and biopsy was advanced with respect to rapidity and sensitivity of detection in mice. Finally, for angiogenesis, an essential microanatomical biomarker of tumor and cardiovascular disease progression, integrin-targeted GNBs allowed visualization of numerous angiogenic sprouts and bridges that were otherwise undetectable from inherent blood signal alone, offering sensitive and specific discrimination and quantification of angiogenesis *in vivo*. Copyright © 2011 John Wiley & Sons, Ltd.

**Keywords:** photoacoustic imaging; gold nanoparticle; fibrin; angiogenesis; sentinel lymphnode; thrombus

## 1. INTRODUCTION

Recently, photoacoustic imaging (PAI) and tomography (PAT) have been of particular interest because of their satisfactory spatial resolution and high soft tissue contrast (1–6). The merits of optical and ultrasonic imaging methods are combined in this novel, hybrid and nonionizing imaging modality. The technique is sensitive to the optical absorption of biological tissue proteins, particularly hemoglobin in circulating erythrocytes. Briefly, tissue is irradiated with a short-pulsed laser beam and protein absorption of optical energy causes thermoelastic expansion and radiates photoacoustic (PA) waves. A clinical, wide-band ultrasonic transducer receives (only) the PA waves and an image is formed without the usual acoustic speckle associated with interactions of transmitted and returning acoustic waves. Because PAT is sensitive to physiological parameters, such as the concentration and oxygenation of hemoglobin, it has the potential to provide unique functional and molecular imaging data *in vivo*. PAT has been used for imaging and quantifying the overall levels of vascularization and oxygen saturation in tumors (1–5), particularly in association with angiogenesis and hypoxia accompanying malignant cancers (7,8).

A major unexplored task has been the development of contrast agents for PA molecular imaging application. Recently, several groups have suggested a number of contrast agents for PAT (2,9,10), but only a few were shown to have the potential for targeted imaging. The prerequisite features beyond the quality of the homing ligand include strong contrast enhancement beyond the endogenous blood signal, *in vivo* particle

biocompatibility and stability during circulatory transit and imaging, and tolerance to sterilization processing.

Gold nanoparticles, because of their optical properties, are an excellent choice for PAT imaging applications and have been well exploited (11–13). Gold particles are excitable in the near-infrared (NIR) range within the 'optical transmission window' of biological tissues ( $\lambda = 650\text{--}900\text{ nm}$ ), which allows for deeper light penetration, lower autofluorescence and reduced light scattering. A major advantage of gold particles is their resistance to photobleaching in contradistinction to small molecule fluorophores that can also be excited in the NIR range using single- or two-photon excitation (11–13). In this review, we discuss the development of a family of colloidal gold nanobeacons (GNB) (14–17) for specific nanomedicine applications.

\* Correspondence to: D. Pan, Division of Cardiology, Campus Box 8215, 660 Euclid Ave, Washington University School of Medicine, St Louis, MO 63108, USA. E-mail: dpan@dom.wustl.edu

a D. Pan, S. A. Wickline, G. M. Lanza  
Department of Medicine, Washington University School of Medicine, St Louis, MO 63108, USA

b M. Pramanik, S. A. Wickline, L. V. Wang, G. M. Lanza  
Department of Biomedical Imaging, Washington University, St Louis, MO 63130, USA

<sup>†</sup> This article is published in *Contrast Media and Molecular Imaging* as part of the special issue on *Photoacoustic Imaging*, edited by Dr. Gregory Lanza, Department of Medicine, Washington University Medical Hospital.

## Biographies

**Dr Dipanjan Pan** is an Assistant Professor of Medicine at the Division of Cardiology, Washington University in St Louis, and has published over 50 original publications, numerous abstracts and patents in the area of materials science, chemistry and nanotechnology. He received his Ph.D. in Synthetic Chemistry from the Indian Institute of Technology, Kharagpur, India in 2002 and pursued a postdoctoral career in polymer science and technology at the Department of Chemistry, Washington University in St Louis. In 2005, he joined General Electric and worked as a part of the global research team supporting the development of their biosciences initiatives. Dr Pan joined the WU faculty in 2007. Subsequently, he co-invented several nanoparticle platforms for molecular imaging application with CT, MRI, optical and photoacoustic imaging. His research is broadly aimed at understanding and developing novel lipid-based and polymeric nanoparticle platforms for molecular imaging, drug delivery and nonviral gene delivery applications with a focus on structure, function and engineering processes. His multidisciplinary approaches encompass a variety of chemical, polymeric, molecular biological and analytical methods to address issues related to cardiovascular and cancer diseases. More specifically, the current inquiries also address the design, synthesis and characterization of nanoscopic materials and contribute to the overall research orientation of the Consortium for Translational Research in Advanced Imaging and Nanomedicine (C-TRAIN). He presently serves as an editorial board member of the *Journal of Biotechnology and Biomaterials* (OMICS) and *World Journal of Radiology* (Baishideng Publishing).



**Manojit Pramanik** received his B.Tech. degree from the Department of Electrical Engineering of the Indian Institute of Technology, Kharagpur, India, in 2002 and M.Tech. degree in Instrumentation Engineering from Indian Institute of Science, Bangalore, India, in 2004. He was awarded his doctoral degree (Ph.D.) from the Department of Biomedical Engineering at Washington University in St Louis in 2010. His research interest is in the area of early breast cancer detection using the principle of thermoacoustic and photoacoustic tomography.



**Samuel A. Wickline** is Professor of Medicine, Physics, Biomedical Engineering, and Cell Biology and Physiology at Washington University. He received his B.A. degree from Pomona College, Claremont, CA in 1974 and his M.D. degree from the University of Hawaii School of Medicine, Honolulu, HI, in 1980. He completed post-doctoral training in Internal Medicine and Cardiology at Barnes Hospital, St Louis, MO in 1987 and joined the faculty of the School of Medicine in the Cardiovascular Division before becoming Director of the Cardiovascular Division at Jewish Hospital and subsequently Co-Director of the Cardiovascular Division at Barnes-Jewish Hospital. He is Co-Director of the Cardiovascular Bioengineering Graduate Program at Washington University and a member of the executive faculty of the Institute for Biological and Medical Engineering. He established the Washington University C-TRAIN at the St Louis CORTEX Center, devoted to diagnostic and therapeutic development of nanotechnology in concert with corporate and academic partners for broadbased clinical applications. He also directs the 'Siteman Center For Cancer Nanotechnology Excellence' at Washington University. Dr Wickline is a founder of two local biotech startup companies in St Louis: Kereos Inc., a nanotechnology startup company devoted to molecular imaging and targeted therapeutics, and PixelEXX Systems Inc., a company that makes semiconductor nanoarrays for molecular diagnostics and microscopy. He also directs the new St Louis Institute of Nanomedicine, a consortium of academic and commercial partners devoted to enhancing regional infrastructure for the translational advancement of nanotechnology in medicine. He is the author of over 200 research papers, and holds more than 50 issued or filed US patent applications.



**Lihong Wang** holds the Gene K. Beare Distinguished Professorship at Washington University. His book, entitled *Biomedical Optics: Principles and Imaging*, won the Joseph W. Goodman Book Writing Award. Professor Wang has published more than 250 peer-reviewed journal articles and delivered more than 270 keynote, plenary or invited talks. He has received 27 research grants as the principal investigator with a cumulative budget of more than \$30 million. His laboratory developed functional photoacoustic CT/microscopy. His Monte Carlo model of photon transport in tissue is used worldwide. He is a Fellow of the AIMBE, OSA, IEEE and SPIE. He serves as the Editor-in-Chief of the *Journal of Biomedical Optics*.



**Dr Lanza** is Professor of Medicine and Bioengineering at Washington University in St Louis, and has 200 original publications, as well as abstracts, chapters and patents across multiple disciplines. He received his Ph.D. from the University Of Georgia School of Agriculture and joined Monsanto Company in 1981, where he established and directed the preclinical research program supporting the development of a 14-day parenteral, controlled release product that is marketed today as Posilac®. In 1988, Dr Lanza matriculated at Northwestern University Medical School in Chicago, where he received an M.D. degree in 1992. He developed expertise in ultrasonic imaging and patented the first acoustic molecular imaging agent. He completed his residency in Internal Medicine and fellowship in Cardiology at Barnes-Jewish Hospital at Washington University School of Medicine. In 1994, as a fellow, he co-invented a new perfluorocarbon based, ligand-targeted contrast agent, which has been broadly patented for use as a multimodality molecular imaging agent as well as for a targeted



drug delivery platform. Dr Lanza joined the Washington University faculty in 1999. Subsequently, he has co-invented numerous nanoparticle platforms for molecular imaging with MRI, ultrasound, CT, optical and photoacoustics. In addition, he has developed nanoparticle platforms and compatible prodrugs to address a variety of unmet medical needs in cardiovascular disease, cancer and arthritis. Dr Lanza is the recipient of numerous awards for research excellence. He is an established principal investigator of the NIH and he is co-Director of C-TRAIN, where his research continues to focus on developing new nanomedicine tools and converting these tools into translatable solutions for medical problems.

## 2. FIBRIN IMAGING *IN VITRO* WITH GOLD NANOBEACONS

Our premise underpinning the development of PAT GNB was to entrap numerous very small gold nanoparticles (2–4 nm) within a larger colloidal particle with a biocompatible phospholipid surfactant similar to that used for other exogenous contrast agents developed in our laboratories. The entrapment of numerous small gold particles was expected to greatly amplify the signal for each binding event, effectively similar to a larger single gold particle, without exceeding the renal elimination threshold size of approximately 6 nm.

The synthesis of the initial gold nanobeacon (GNB-M) entailed suspension of octylthiol-coated spherical gold nanoparticles (AuNPs, 2 w/v%), in almond oil (20 vol%) followed by microfluidization of the mixture with phospholipid surfactants (2%,

w/v) (Fig. 1). The surfactant mixture comprised phosphatidylcholine (PC, 91 mol%) and cholesterol (8 mol%) and included biotin-caproyl-PE (1 mol%) or a phospholipid-anchored homing ligand (0.3–1.0 mol%) at the equimolar expense of PC depending on the research application. The GNB-M particles were  $154 \pm 10$  nm with polydispersity and  $\zeta$ -potential of  $0.08 \pm 0.03$  and  $-47 \pm 7$  mV, respectively (Brookhaven Instrument Co.). Gold content, determined by ICP-MS, was  $1080 \mu\text{g/g}$  of the 20% colloid suspension. UV-vis spectroscopy confirmed the absorbances at  $\sim 520$  nm and in the NIR window ( $\sim 900$  nm). The particle size and  $\zeta$ -potential of GNB-M varied less than 5% over 100 days when stored at  $4^\circ\text{C}$  under argon in sealed serum vials.

GNB-M were initially evaluated in suspension and homed to acellular fibrin-rich clots *in vitro* to assess background blood pool effects and targeted contrast potential, respectively (14). The PA signal from a 20% GNB suspension mixed 1:1 with rat blood

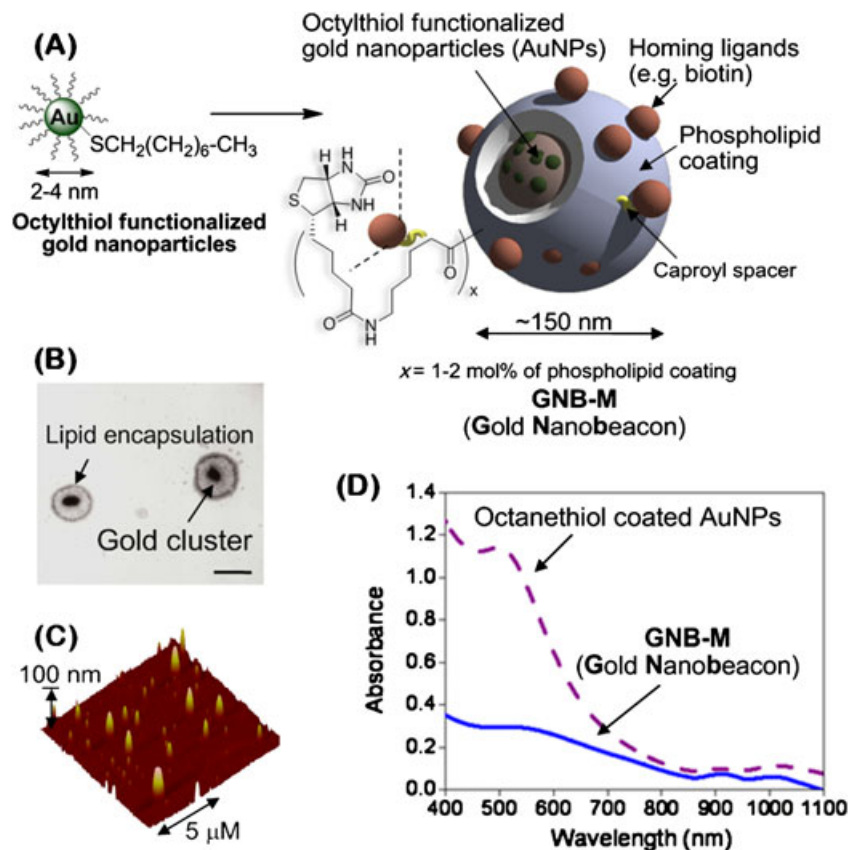


**Figure 1.** (A) Preparation of gold nanobecons from octanethiol-functionalized gold nanoparticles (AuNPs).  $x = 1\text{--}2$  mol% phospholipid coating. (B) Transmission electron microscopy image of gold nanobecons (drop deposited over nickel grid, 1% uranyl acetate; scale bar: 100 nm). (C) Atomic force microscopy image of gold nanobecons. Average height  $H_{av} = 10151$  nm. (D) UV-vis spectroscopic profile. Solid blue line, gold nanobecons; purple dashed line, octanethiol-coated AuNPs. Spectra are not normalized. [Reproduced with permission from Pan *et al.* (14)].

within Tygon® tubing (i.d. 250  $\mu\text{m}$ , o.d. 500  $\mu\text{m}$ ) was 15 times stronger than that from pure rat blood. Averaged over the entire 740–820 nm NIR window, the PA signal enhancement by GNB over blood was greater than 10-fold (Fig. 2).

While enhanced blood pool imaging is an opportunity for GNB, the inherent contrast from hemoglobin alone or augmented by other optically absorptive compounds, such as methylene blue, is usually adequate for such clinical applications. However, high contrast in the presence of blood is requisite for GNB-M molecular imaging of fibrin within intraluminal microthrombus associated with ruptured atherosclerotic plaques.

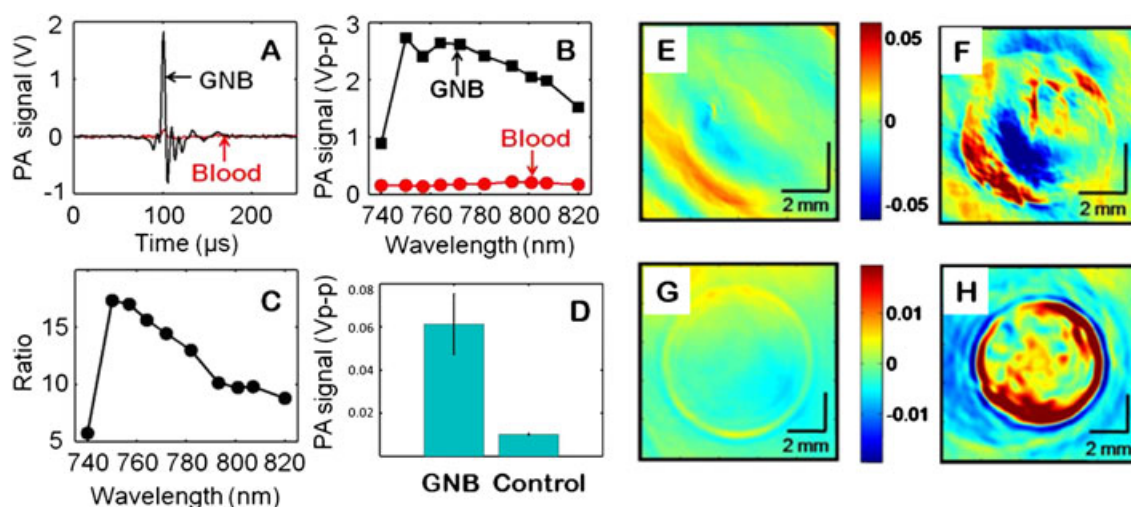
Fibrin is an abundant and unique component of intravascular thromboses. GNB-M and the control nanobeacons (i.e. containing no metal) were targeted to acellular fibrin clot phantoms with classic avidin–biotin coupling using a well-characterized biotinylated anti-human fibrin-specific monoclonal antibody (NIB5F3) (18). The clots in low-density polyethylene tube ( $\sim 1\text{ cm}^3$  volume, i.d.  $\sim 6\text{ mm}$ ) were targeted with biotinylated GNB and control (targeted, nonmetallic nanobeacon). Figure 2(E and F) shows cross-sectional PAT images using a curved array PAT system (19) with an 800 nm wavelength laser. High contrast was clearly seen for GNB targeted clots in comparison to the control clot targeted with nonmetallic nanoparticles.

Figure 2(G and H) shows cross-sectional PAT images, using a PA breast scanner system (20), of the same control and targeted plasma clots, respectively (14). For this system, a 532 nm wavelength laser source was used. As expected, the targeted plasma clot was clearly visible (Fig. 2F) in the PAT image, whereas the control clot image was not detectable (Fig. 2E). This imaging result was supported analytically by total gold content analyses. The total gold contents of the clots with targeted GNB-M, nontargeted GNB-M and targeted nonmetallic nanobeacons were found to be 47  $\mu\text{g/g}$ , not detected (ND,  $<0.02\text{ }\mu\text{g/g}$ ) and ND respectively, by ICP-MS. These *in vitro* images along with analytical supporting data illustrated the concept of intravascular PA with GNB-M.

### 3. GOLD NANORODS AS ALTERNATIVE TO SPHERICAL NANOPARTICLES

We explored the opportunity for manipulating gold particle shape to improve photoacoustic contrast enhancement. Rod-shaped gold nanoparticles (i.e. nanorods) offer distinct optical properties resulting from two surface plasmon (SP) bands corresponding to the transverse and longitudinal SP bands in the visible ( $\lambda = 520\text{ nm}$ ) and the NIR ( $\lambda = 900\text{ nm}$ ) regions, respectively (11–13). Owing to the intrinsic large extinction coefficient of longitudinal band, rods are often used as probes for fluorescence, light scattering and two-photon luminescence imaging. However, the longitudinal SP bands are very sensitive to the aggregation of gold nanorods. The peak positions of the SP bands depend on the anisotropic shape of each gold nanorod; the aggregation of rods generates isotropic (random) coupling of SP oscillations, and produces dramatic changes of the longitudinal SP bands. Owing to these properties, gold nanorods are expected to provide a good contrast for photoacoustic imaging using the near-IR region.

The design of the self-assembled gold nanorod (GNB-R) nanoparticles was based on the self-assembly of natural amphiphiles in aqueous media to entrap hundreds of gold atoms (16). Polymer-coated gold nanorods (GNR; transmission electron microscope axial diameter,  $25 \pm 5\text{ nm}$ ; length,  $80 \pm 8\text{ nm}$ ; Longitudinal Surface Plasmon Resonance (LSPR), 750 nm; Transverse Surface Plasmon Resonance (TSPR), 530 nm; Fig. 1A) were dispersed in chloroform and premixed with vegetable oil (20% v/v almond oil) core matrix. The chloroform was removed under reduced pressure at 45  $^\circ\text{C}$  to form a suspension of gold nanorods in vegetable oil-based core matrix. In a parallel step, phospholipids were dissolved in chloroform, filtered and evaporated to dryness under reduced pressure to form a lipid–thin film mixture. The surfactant mixture comprised PC (99 mol%) and biotin–caproyl–PE (1%) for *in vitro* evaluation. Lipid thin film mixture was dispersed in water (0.2  $\mu\text{m}$ ) and homogenized with the GNB-R suspension at 20 000 psi for 4 min to produce self-assembled gold nanorods (Fig. 3). The



**Figure 2.** (A) Photoacoustic (PA) signals generated from a Tygon® tube (i.d. 250  $\mu\text{m}$ , o.d. 500  $\mu\text{m}$ ) filled with gold nanobeacons (GNB) and rat blood. The excitation light is of 764 nm wavelength. (B) PA spectrum of GNB and blood over a 740–820 nm range of near-infrared wavelengths. (C) Ratio of the peak-to-peak PA signal amplitudes generated from GNB to those of blood. (D) PA signal-to-noise ratio for the GNB and the control (no gold). Cross-sectional PA image of a low-density polyethylene tube ( $\sim 1\text{ cm}^3$  volume, i.d.  $\sim 6\text{ mm}$ ) filled with plasma clot: (E) control, (F) targeted with GNB using a curved array PA system ( $\lambda = 800\text{ nm}$ ). (G) Control, (H) targeted with GNB using a photoacoustic breast scanner system ( $\lambda = 532\text{ nm}$ ). [Reproduced with permission from Pan *et al.* (14)].

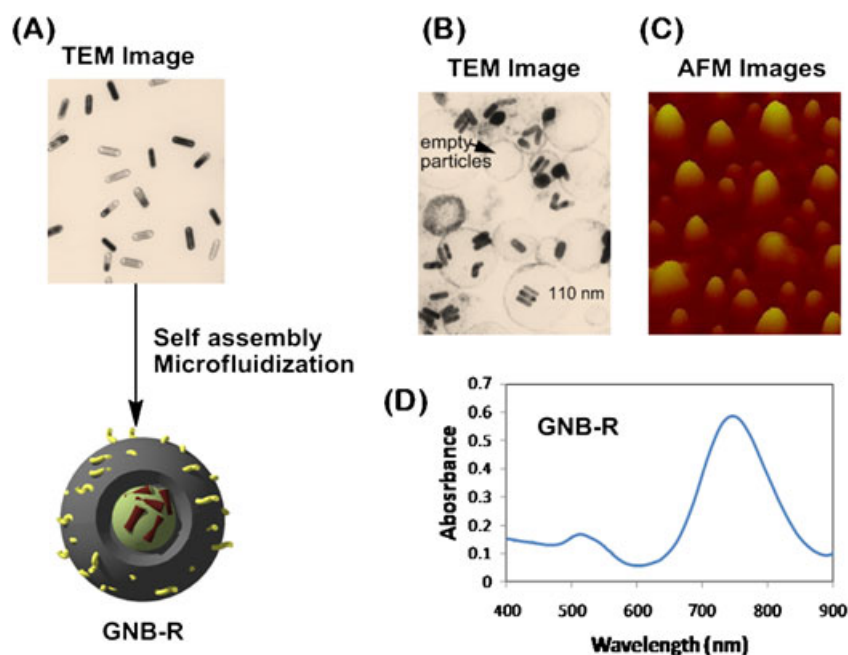


**Figure 3.** (A) Transmission electron microscopy (TEM) image of gold nanorods drop deposited over Ni-grid; (B) TEM images of gold nanorod (GNB-R) drop deposited over Ni-grid; (C) atomic force microscopy images of GNB-R drop deposited over glass; (D) UV-vis spectrum of gold nanorods showing LSPR and TSPR bands at 750 and 530 nm, respectively. [Reproduced with permission from Pan *et al.* (16)].

particle thus formed was immediately subjected to dialysis against nanopure water using cellulosic membrane (20 kDa Molecular Weight Cut Off (MWCO)).

This synthesis resulted in an encapsulation of  $\sim 127$  gold metal atoms (ICP-MS =  $8.12 \mu\text{g}$  of gold/g of 20% colloidal nanobeacon), markedly less than GNB-M. The GNB-R particles had a nominal hydrodynamic diameter of  $129 \pm 7$  nm as measured by dynamic light scattering (DLS). The polydispersity and  $\zeta$ -potential were measured as  $0.06 \pm 0.02$  and  $-41 \pm 12$  mV (Brookhaven Instrument Co.), respectively. The large negative  $\zeta$ -potential implied successful phospholipid encapsulation and high colloidal stability of these nanoparticles. The dehydrated state diameter ( $D_{av}$ ) and height parameters ( $H_{av}$ ) of the GNB-R were  $105 \pm 28$  and  $60 \pm 24$  nm, as measured by transmission electron microscopy (TEM) and atomic force microscopy (AFM) measurements, respectively (Fig. 3B and C). The discrepancies in hydrodynamic diameter (DLS) and height values (AFM) was presumably due to the partial flattening of the nanoparticles on the glass substrates, which is indicative of the soft, compressible nature of these nanoparticles. TEM images of the GNB-R confirmed the presence of multiple gold nanorods within the phospholipid-encapsulated particles (16). AFM images pointed towards the spherical nature of the particles. However, in contradistinction to GNB-M, the low encapsulation efficiency of the gold rods resulted in low concentrations of metal per GNB-R with less blood pool contrast (approximately 3-fold). Moreover, the size of large gold nanorods would probably preclude bioelimination through a renal route in nonrodent mammals. Consequently, subsequent studies utilized minute spherical gold nanoparticles, as used in GNB-M.

#### 4. SENTINEL LYMPHNODE IMAGING

Today patients with breast cancers typically undergo invasive sentinel lymph node (SLN) biopsy to rule out metastatic disease.

In an experienced surgeon's hands the effectiveness of this technique can be very good but, not infrequently, the recovery of lymph nodes (LNs) is less than desired and the sentinel LN is missed (21,22). Moreover, SLN biopsy is frequently associated with complications, including local seroma formation, lymphedema, nerve injury and reduced range of motion of arms (23). Noninvasive molecular techniques for axillary staging for breast cancer in conjunction with minimally invasive percutaneous fine-needle biopsy (FNAB) offer a marked advancement over invasive exploration and resection. Photoacoustic nanoparticle-based contrast agents with high contrast enhancement injected subcutaneously can migrate into lymphatics and travel to the sentinel LNs, and can be detected at depths of 4–5 cm. (Please refer to the lead article in this issue by Junjie Yao and Lihong Wang for an in-depth discussion with specific examples on this topic.) While the material nature of PAT nanoparticles is often a prime consideration for investigators developing contrast agents, we reported in these studies the crucial influence of size and mass.

We initially studied the effectiveness of GNB-M distribution into sentinel lymph nodes following subcutaneous injection in a rodent model (15). A sagittal maximum amplitude projection (MAP) photoacoustic image of the axillary area clearly delineates the vasculature by virtue of the light-absorbing red blood cells with high spatial resolution of  $\sim 500 \mu\text{m}$ . Note also that the normal speckle pattern seen in ultrasound images owing to the additive and cancelling interference pattern of transmitted and reflected acoustic waves was not observed, since PAT utilizes ultrasound only in a receive mode. After the baseline image was acquired, GNB-M were injected intradermally into the rat forepaw and dynamic PA images were acquired. Within 5 min, GNB-M was found to have accumulated in the SLN and also in adjacent secondary LN. While the signal was strong, the consensus was to try for a more robust contrast. One approach, 'bigger is better', led to the development and testing of a larger

PA agent with substantially more gold per particle than GNB-M, a polymer encapsulated gold nanobeacon (GNB-L).

In a typical synthesis of GNB-L, a di-block co polymer (polystyrene-*b*-polyacrylic acid) PS-*b*-PAA (24–27) ( $M_n \times 10^3$ : 0.8-*b*-29.3, polydispersity index=1.18, 0.0033 mmol) was dissolved in a mixture of methanol and  $\text{CHCl}_3$  (4:1) and subjected to controlled evaporation under reduced pressure to generate a thin film of polymer. The thin film was dispersed in deionized water (0.2  $\mu\text{m}$ ) by probe sonication at ambient temperature. Octanethiol-coated AuNPs (2 w/v%) were suspended in polysorbate (sorbitan monolaureate, 5 vol%, and microfluidized with PS-*b*-PAA dispersion (0.5 vol%) yielding a 10% colloidal suspension of nanoparticles (Fig. 4). The nanobecons were purified by exhaustive dialysis against infinite sink of nanopure water using cellulosic dialysis membrane (20 kDa MWCO). GNB-L (289  $\pm$  24 nm) had a narrow distribution (polydispersity index, 0.15  $\pm$  0.04). The particle stability and successful amphiphilic-encapsulation were confirmed based on the presence of negative electrophoretic potential ( $\zeta$ ) values. In contradistinction to the gold content of GNB-M (6120 metal atoms/particle), each GNB-L contained 71,493 gold metal atoms per nanobeacon. PA contrast in a 1:1 (v/v) blood to GNB-L emulsion mixture produced a strong PA signal, significantly greater than that of GNB-M (15).

As described for GNB-M, baseline control images revealed the microvasculature surrounding the unvisualized LN (Fig. 5B). Injection of GNB-L into the rat forepaw followed by serial examination with PA revealed no detectable signal over the anticipated course of the imaging session (Fig. 5D). Moreover, re-examination of the LN territory over the next 3 days showed no migration to and uptake of GNB-L by the sentinel lymphnode. Therefore, despite a marked enhancement in gold content and PA signal contrast, GNB-L was ineffective for LN imaging. We hypothesized that the larger size and or mass of GNB-L led to poor migration and uptake of the particles by the

lymphatic system. Given this result, a third smaller gold nanobeacon (GNB-S), was produced and evaluated (15).

GNB-S was prepared by retuning to the matrix and surfactants of GNB-M (Fig. 4). Briefly, oleate-coated AuNPs (2 w/v% of inner matrix, 2–4 nm) were suspended in polysorbate (sorbitan monolaureate, 20 vol%) and homogenized with a surfactant mixture, resuspended from a lipid film, at 137.9 MPa (i.e. 20 000 PSI (pound per square inch (pascal)) for 4 min. The surfactant mixture mainly comprised PC (92 mol% of lipid constituents) and cholesterol (8 mol%). Hydrodynamic particle size for GNB-S was 92  $\pm$  12 nm with a polydispersity index of 0.35  $\pm$  0.05. The  $\zeta$ -potential ( $\zeta$ ) was  $-35 \pm 8$  nm, confirming appropriate particle encapsulation. Gold metal atom content per particle was determined to be nine gold metal atoms per GNB-S particle, vastly lower than GNB-M or GNB-L. Suspended in blood, GNB-S, peak-to-peak PA signal amplitude ( $\lambda = 767$  nm) was 168  $\pm$  12 mV, slightly higher than that of blood (133  $\pm$  7 mV) and markedly less than that of GNB-L (540  $\pm$  30 mV).

In the rat sentinel lymphnode model, the microvasculature at baseline was again clearly visible (marked with red arrows) while the lymph node, devoid of optical absorbers, was not seen. After the control image was acquired, GNB-S was injected intradermally into the forepaw of the rat and the acquisition of dynamic PA images proceeded. Figure 5(F and G) shows two MAP images of the same axillary area 5 and 20 min after the GNB-S injection, respectively, with the SLN as a bright spot (green arrow), and dramatically more robust than was observed with GNB-M or the larger GNB-L. Moreover, GNB-S was seen clearly in transit within the lymphatic ductile and accumulated in the sentinel lymphnode at 5 min post-injection. After 10–15 min of injection the GNB-S had completed migrated through the lymphatic ductile and a persistent and robust signal from the lymph node was detected over the next hour. The contrast of the sentinel LN to the surrounding blood vessel was 9:1 (ratio of the peak-to-peak PA signal amplitude obtained from the blood vessel and SLN) after

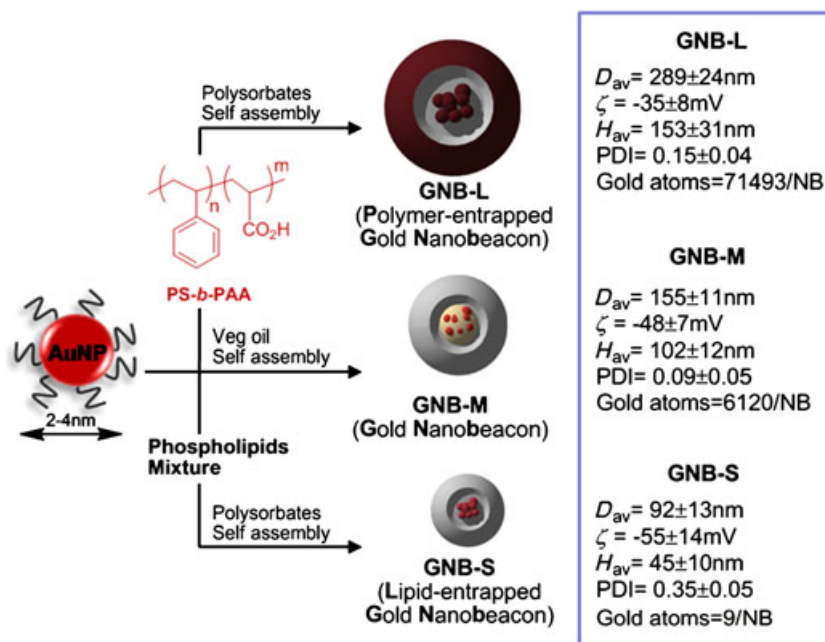


**Figure 4.** Synthesis of gold nanobecons.  $D_{av}$ , Number averaged (dynamic light scattering, DLS);  $\zeta$ , electrophoretic potential;  $H_{av}$ , average height (atomic force microscopy); PDI, polydispersity index (DLS). [Reproduced with permission from Pan *et al.* (15)].

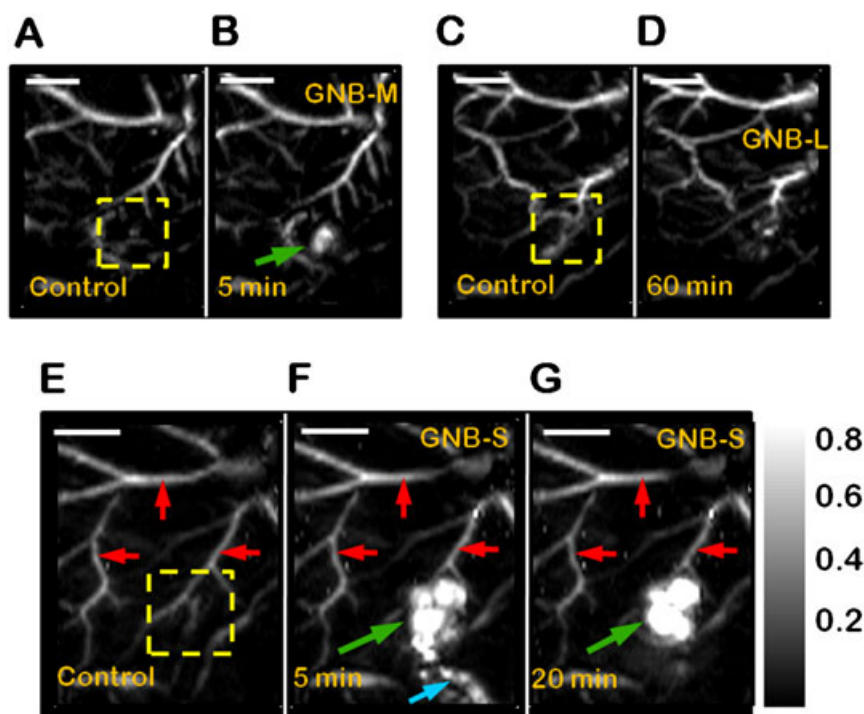


**Figure 5.** *In vivo* noninvasive photoacoustic imaging of sentinel lymph nodes in rat ( $\lambda = 767$  nm). (A–G) Scale bar is 5 mm. Aliquots of 150  $\mu$ l of nanobeacons were injected intradermally in all cases. GNB-M: (A) control PA image; (B) 5 min post-injection image of GNB-M (5  $\mu$ M). GNB-L: (C) control PA image; (D) lymph node is not visible in a 60 min post-injection image of GNB-L (680 nM). GNB-S: (E) sagittal maximum amplitude projection (MAP) (28) pre-injection control image; bright parts represent optical absorption from blood vessels, marked with red arrows; (F) PA image (MAP) acquired 5 min after GNB-S injection (10 nM); SLNs are clearly visible, marked with green arrows; lymphatic vessel is also visible, marked with blue arrows; (G) 20 min post-injection PA image. [Reproduced with permission from Pan *et al.* (15)].

GNB-S injection. Unlike GNB-M and GNB-L, which would be constrained by size to the vasculature, GNB-S diffused into surrounding blood vessels, as was evident from the increased PA signal in the capillaries. The above experiment was successfully repeated with diluted GNB-S (2.5 and 1 nM) (15).

In summary, both GNB-M and GNB-S functioned as contrast agents for PA sentinel lymphnode imaging in the NIR window; however the smaller GNB-S, with fewer gold particles per nanoparticle, markedly outperformed the larger GNB contrast agents. These data illustrate the importance of refining PA contrast design for each intended application.

## 5. INTEGRIN-SPECIFIC PHOTOACOUSTIC IMAGING OF ANGIOGENESIS

Angiogenesis is an essential microanatomical component of tumor and cardiovascular progression that may be effective as a quantitative indicator of tumor or cardiovascular plaque progression or response to therapy (29–31). The  $\alpha_v\beta_3$ -integrin, a heterodimeric transmembrane glycoprotein, is expressed by numerous cell types, including endothelial cells (32), macrophages (33), platelets (34), lymphocytes (35), smooth muscle cells (36) and tumor cells (37,38). Fortunately, the steric constraint of perfluorocarbon nanoparticles to the vasculature precludes significant interaction with nonendothelial integrin-expressing cells, which greatly enhances neovascular target specificity (39). Although PAT generates high-resolution images of red blood cells in the microvasculature (40–46), hemoglobin imaging does not discriminate immature neovasculature and mature microvessels. The

adjunctive of an angiogenesis-specific molecular PA imaging agent not only resolved red blood cell-containing angiogenic vessels from similar but more mature microvessels, but also revealed the presence of neovascular sprouts forming and bridging between neovessels.

To date, photoacoustic contrast agents targeting angiogenesis have been designed around integrin-targeted indocyanine green (ICG)-fluorescent-peptide conjugates (47–51). Unfortunately these agents easily diffuse from the neovascular vasculature, where numerous cell types including macrophages, platelets, lymphocytes, smooth muscle cells and tumor cells express  $\alpha_v\beta_3$  integrin. In the present study, GNB-M precluded microscopically detectable extravasation beyond the 'leaky' neovasculature of the Matrigel™ plug. This observation was further supported by other reports using copolymer and nanoemulsion particles (39,52). Such steric constraint with  $\alpha_v\beta_3$ -GNB-M nanoparticles greatly enhanced neovascular homing specificity, which will be essential for quantitative biomedical applications.

The  $\alpha_v\beta_3$ -targeted GNB-M was selected for study (17) for vascular constraint properties owing to its particle size (160 nm), as opposed to GNB-S (90 nm), with a high potential for extravasation or GNB-L (290 nm), which would have a shorter half-life owing to its mass and size. The  $\alpha_v\beta_3$ -targeted GNB-M was produced by microfluidization as discussed before with a surfactant mix comprising phosphatidylcholine (91.9 mol%), cholesterol (8 mol%) and an  $\alpha_v\beta_3$ -peptidomimetic antagonist conjugated to PEG<sub>2000</sub>-phosphatidylethanolamine (0.1 mol%, Kereos Inc., St Louis, MO, USA) (53). The  $\alpha_v\beta_3$ -integrin antagonist was a quinalone nonpeptide developed by Lantheus Medical Imaging (US patent 6,511,648 and related patents). The

vitronectin antagonist was initially reported and characterized as the  $^{111}\text{In}$ -DOTA conjugate RP478 and cyan 5.5 homolog TA145 (54). The specificity of the  $\alpha_v\beta_3$ -ligand mirrors that of the anti  $\alpha_v\beta_3$ -LM609 antibody (55) (Chemicon International Inc., Billerica, MA, USA) as assessed by staining and flow cytometry. The  $\text{IC}_{50}$  for  $\alpha_v\beta_5$ ,  $\alpha_5\beta_1$  and GP IIb/IIIa was determined to be  $>10\ \mu\text{m}$  (Lantheus Medical Imaging, Billerica, MA, USA, unpublished data).

A Matrigel™ plug model of angiogenesis was used (BD Biosciences, San Jose, CA, USA). Matrigel™ (750  $\mu\text{l}$ ) enriched with fibroblast growth factor-2 (500 nm/ml; Sigma Aldrich, St Louis, MO, USA) and heparin (64 U/ml) was implanted subcutaneously along the flank of mice. PAT imaging was performed prior to treatment and serially over 5 h post-injection on days 16 and 17 post-implantation. Animals were randomly distributed into four groups and received: (1)  $\alpha_v\beta_3$ -gold nanobeacons ( $\alpha_v\beta_3$ -GNB-M,  $n=6$ ); (2)  $\alpha_v\beta_3$ -nanobeacons without gold ( $\alpha_v\beta_3$ -NB) followed by  $\alpha_v\beta_3$ -GNB-M (competitive blockage,  $n=2$ ); (3) nontargeted gold nanobeacons (NT-GNB-M,  $n=3$ ) or (4) saline ( $n=2$ ).

Two parameters were calculated from the PAT images: the number of pixels of hemoglobin in blood vessels and the photoacoustic signal amplitude in those pixels. An angiogenesis index was created and defined as the cross-product of blood vessel pixel number and total photoacoustic signal from those pixels. The data for each PA acquisition were normalized to the pretreatment (baseline) to create a normalized angiogenesis index of each animal. PA signal changes in the Matrigel™ plug were monitored serially over 5 h or more (Fig. 6).

Briefly, noninvasive PAT of angiogenesis using a 10 MHz ultrasound receiver with  $\alpha_v\beta_3$ -GNB-M produced a 600% increase in signal in a Matrigel™ plug mouse model relative to the inherent hemoglobin contrast pretreatment. In addition to increasing the contrast of neovessels detected at baseline,  $\alpha_v\beta_3$ -GNB-M allowed visualization of numerous angiogenic sprouts and bridges that were undetectable before contrast injection. Competitive inhibition of  $\alpha_v\beta_3$ -GNB-M with  $\alpha_v\beta_3$ -NB almost completely blocked contrast enhancement to pretreatment

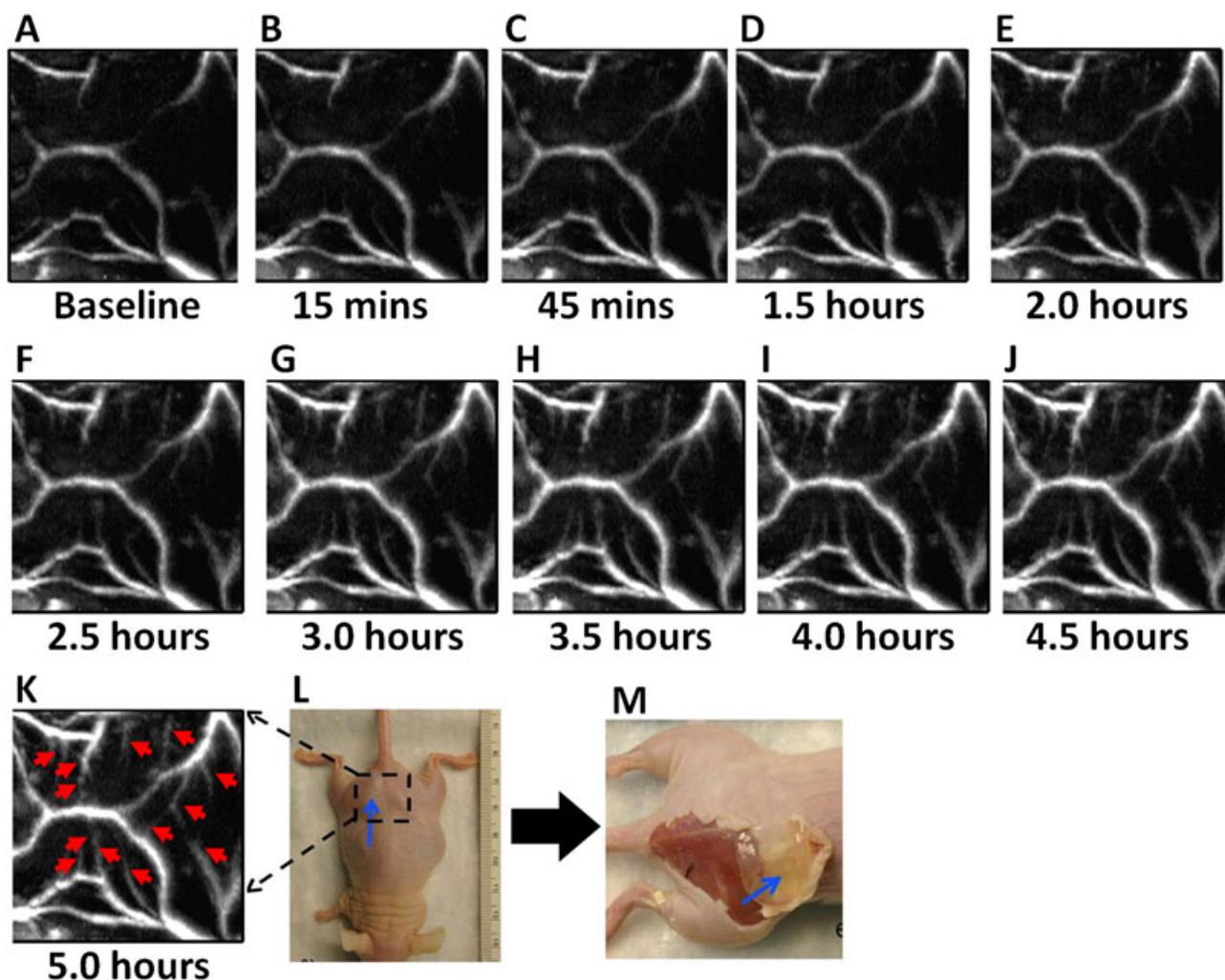


**Figure 6.** A 0.75 ml aliquot of Matrigel™ was implanted subcutaneously in a nude mouse. The mouse was imaged photoacoustically 8–20 days after Matrigel™ implantation. (A) Photoacoustic (PA) maximum amplitude projection (MAP) image of the dotted area. This is a control image. After the control image was taken, targeted gold nanobeacons ( $\alpha_v\beta_3$ -GNB-M) were injected intravenously using the tail vein. In a time course study (B–K), PA images were acquired with an interval of approximately 0.5 up to 5 h. (G) Three hours post-injection PA image. Red arrows point to the angiogenic sprout (not visible in A). (K) Five hours post-injection PA image. For all PA images  $\lambda=767\ \text{nm}$ , scale bar = 5 mm. (L) Digital photograph of a mouse implanted with Matrigel™ plug. Blue arrow points to the plug. The black dotted area was imaged. The smallest tick was 1 mm. (M) Digital photograph of the sacrificed mouse after all the image acquisition was completed. The skin has been removed to show the Matrigel™ plug (blue arrow). [Reproduced with permission from Pan *et al.* (17)].

levels, similar to the signal from animals receiving saline only. Consistent with other studies, nontargeted GNB passively accumulated in the tortuous neovascularity, but provided less than half of the contrast enhancement of the targeted agent.

Figure 6 illustrates in native PA images the marked enhancement of angiogenic vessel contrast over time. Individual microvessels observed prior to treatment were markedly enhanced with  $\alpha_v\beta_3$ -GNB-M. Remarkably, an evolving pattern of neovascular bridges between neovessels and budding angiogenic sprouts were easily visualized with noninvasive PAT and  $\alpha_v\beta_3$ -GNB-M that could not be detected at baseline by hemoglobin contrast alone. These developing neovessels were probably too immature and incomplete to support blood flow. Similar images in the saline control animals showed no change in vascular anatomy over the same time course. Indeed these images illustrate the genesis of neovasculature in the Matrigel™ plug model.

Microscopic studies confirmed that the vascular-constrained, rhodamine-labeled  $\alpha_v\beta_3$ -GNB-M homed specifically to immature neovasculature Platelet Endothelial Cell Adhesion Molecule (PECAM<sup>+</sup>, Tie-2<sup>-</sup>) along the immediate tumor periphery, but not to nearby mature microvasculature (PECAM<sup>+</sup>, Tie-2<sup>+</sup>). Figure 7(A) presents a low-power hematoxylin and eosin stain (H&E) stained example of an excised Matrigel™ plug with the muscle and skin labeled for orientation. The red box depicts a region of interest closely approximated to the perimeter of the Matrigel™ depot, which coincides with images in Fig. 7(B–D). The blue box defines a nearby subcutaneous region of interest, which is also depicted in Fig. 7(E–G). Fluorescent microscopy revealed the marked accumulation of rhodamine  $\alpha_v\beta_3$ -GNB-M nanoparticles in the immediate Matrigel™ periphery (Fig. 7B) that was not seen in the adjacent subcutaneous tissue (Fig. 7E).

PECAM staining demonstrated abundant microvasculature in both the red (Fig. 7C) and blue (Fig. 7F) tissue regions. PECAM distribution in Fig. 7(B) is closely aligned with the targeted rhodamine  $\alpha_v\beta_3$ -GNB-M, but microvessels evident in Fig. 7(F) show no decoration with rhodamine nanoparticles. Lac-Z staining, which is regulated by the Tie-2 promoter, is negligible in Fig. 7(D), where  $\alpha_v\beta_3$ -GNB-M is prevalent. Conversely, Tie-2 staining in Fig. 7(G) closely corresponds to the PECAM signal in Fig. 7(F), neither of which is associated with rhodamine  $\alpha_v\beta_3$ -GNB-M. These data indicate that the PA signal observed with  $\alpha_v\beta_3$ -GNB-M was from the forming (PECAM<sup>+</sup>, Tie-2<sup>-</sup>) angiogenic endothelium induced by the Matrigel™ growth factors and not from mature microvessels (PECAM<sup>+</sup>, Tie-2<sup>+</sup>) in the plug periphery. While PAT alone could not differentiate PA signal derived from forming and stabilized neovessels, with  $\alpha_v\beta_3$ -GNB-M contrast enhancement, the PAT sensitively discriminated angiogenesis and microvasculature.

## 6. CONCLUSION AND FUTURE OF PHOTOACOUSTIC TOMOGRAPHY

PAT is a nascent modality with no clinically installed instrument base, yet the prospects are good that this modality will make a significant contribution in biomedical diagnosis in the next decade. The results discussed in this review utilized a clinically appropriate acoustic receiver frequency (10 MHz), although the instrumentation was a laboratory robotic scanner. The first PAT scanners for the preclinical research market are now commercially available, and prototype clinical medical scanners capable of integrating PAT and ultrasound images are being evaluated in the clinic. The time to complete preclinical regulatory requirements

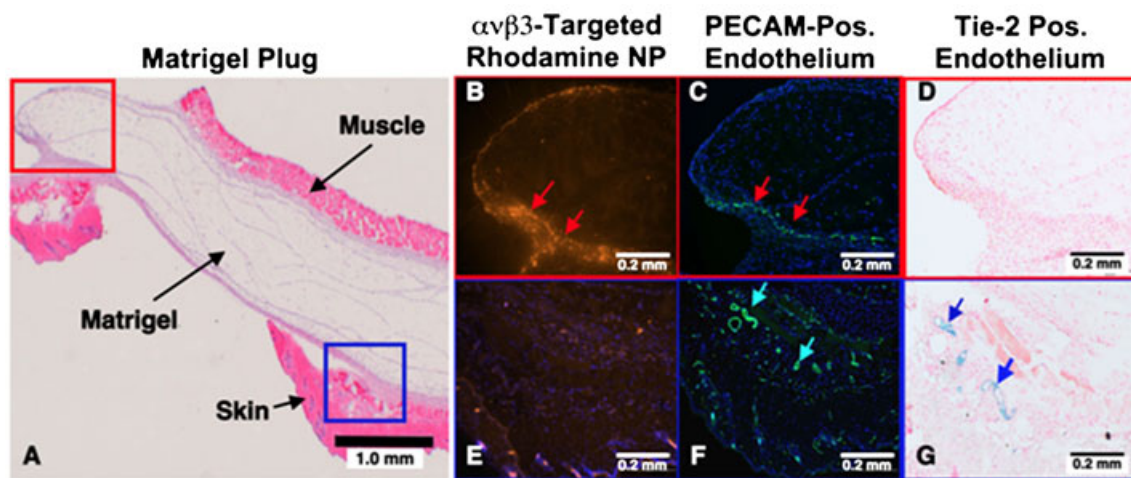


**Figure 7.** Microscopic examination of FGF Matrigel subcutaneous explant from FVB/N-TgN(TIE2LacZ)182Sato mice following injection (i.v.) of  $\alpha_v\beta_3$ -targeted rhodamine labeled GNB-M nanoparticles. These transgenic mice carry a  $\beta$ -galactosidase reporter gene under the control of the murine Tek (Tie2) promoter. LacZ is expressed specifically in vascular endothelial cells in embryonic and adult mice. (A) H&E staining of the excised implant providing spatial orientation of the matrix with respect to skin and muscle. The red box region is further examined in (B–D). The blue box region is studied in more detail in (E–G). (B, E) The accumulation of  $\alpha_v\beta_3$ -targeted rhodamine nanoparticles in the red and blue tissue regions respectively. Note the brilliant and dense accumulation of nanoparticles in (B) (red arrows) and little to no accumulation of particles in the (E) region. (C, F) The staining of vascular endothelium for PECAM (CD34) in the red (C) and blue (F) regions of the matrigel plug. There was dense vascularity in both locations (red arrows in C and turquoise arrows in F). (D, G) depict the LacZ signal for  $\beta$ -galactosidase under Tie2 promoter control. In (D), no LacZ signal was detected, reflecting a paucity of mature microvessels. In contradistinction, there is a strong LacZ signal in (G). These results indicated that the  $\alpha_v\beta_3$ -GNB nanoparticles were specifically targeted to angiogenic endothelial cells (PECAM<sup>+</sup>/Tie-2<sup>-</sup>) and not to more mature microvessels, which were PECAM<sup>+</sup>/Tie-2<sup>+</sup>. The data corroborated that photoacoustic tomography imaging with  $\alpha_v\beta_3$ -targeted GNB specifically distinguished and enhanced the angiogenic neovasculature from new, but more matured and differentiated microvessels. [Reproduced with permission from Pan *et al.* (17)].

for a GNB Investigational New Drug Application Approval is longer than the time required for the instrument to receive an Investigational Device Exemption; perhaps the scanner and the contrast agent can be co-developed to reach the clinic within a close sequential timeframe.

PAT alone or with approved dyes, such as methylene blue, offers significant clinical opportunities by extending the current ultrasound capability to include simultaneous anatomical and functional assessments of tissue vasculature. With the use of GNB-S, the potential for robust sentinel lymphnode assessment and biopsy was greatly improved owing to the dramatic improvement in detection sensitivity, and the rapidity by which the results were obtained. The detection of microthrombus formed over a ruptured atherosclerotic plaque with fibrin-targeted GNB-M, particularly in the carotid territory, offers an important opportunity to recognize patients with moderate lumen stenosis but high risk of stroke; this is a critical unmet need not achievable with current clinical ultrasound techniques (or other noninvasive imaging modality).

Finally, angiogenesis is an essential microanatomical biomarker of tumor and cardiovascular disease progression and intensity as well as a metric of therapeutic responses to therapy. PAT offers a versatile and lower cost methodology to assess the angiogenic status of cancers (including head and neck, breast, skin, prostate, uterine, gastrointestinal and testicular neoplasia) before or after therapy using neovasculature as a marker of aggressive or malignant disease pretreatment, or as an indicator of disease recrudescence. The same paradigm may be applied to carotid or peripheral vascular disease, where angiogenesis can be a direct intramural marker of plaque inflammatory activity and progression, which also acts as an amplifying element leading to lesion instability.

Clearly the opportunities for PAT contributions to healthcare management have only begun to be recognized. The development of this technology is only limited by its availability for research in the laboratory and the clinic. We anticipate that a growing number of laboratories will begin to utilize PAT in research and stimulate demand for clinical translation of the technology.

## REFERENCES

- Wang XD, Pang YJ, Ku G, Xie XY, Stoica G, Wang LHV. *Nat Biotechnol* 2003; 21: 803–806.
- Li ML, Oh JT, Xie XY, Ku G, Wang W, Li C, Lungu G, Stoica G, Wang LHV. *Proc IEEE* 2008; 96: 481–489.
- Wang XD, Xie XY, Ku G, Wang LHV. *J Biomed Opt* 2006; 11: 024015.
- Lungu GF, Li ML, Xie XY, Wang LHV, Stoica G. *Int J Oncol* 2007; 30: 45–54.
- Ku G, Wang XD, Stoica G, Wang LHV. *Phys Med Biol* 2004; 49: 1329–1338.
- Ku G, Wang XD, Xie XY, Stoica G, Wang LHV. *Appl Opt* 2005; 44: 770–775.
- Schneider BP, Miller KD. *J Clin Oncol* 2005; 23: 1782–1790.
- Vaupel P, Mayer A, Briest S, Hockel M. *Oxygen Transport to Tissue XXVI* 2005; 566: 33–342.
- Agarwal A, Huang SW, O'Donnell M, Day KC, Day M, Kotov N, Ashkenazi S. *J Appl Phys* 2007; 102: 064701–064704.
- Zerda AD, Zavaleta C, Keren S, Vaithilingam S, Bodapati S, Liu Z, Levi J, Smith, BR, Ma T-J, Oralkan O, Cheng Z, Chen X, Dai H, Khuri-Yakub BT, Gambhir SS. *Nat Nanotechnol* 2008; 3: 557–562.
- Kojima H, Zasshi Y. Development of near infrared fluorescent probes for near infrared imaging. *Yakugaku Zasshi* 2008; 128: 1653.
- Ntziachristos V, Bremer C, Weissleder R. Fluorescence imaging with nearinfrared light: new technological advances that enable in vivo molecular imaging. *Eur Radiol* 2003; 13: 195.
- Rostro-Kohanloo BC, Bickford LR, Payne CM, Day ES, Anderson LJ, Zhong M, Lee S, Mayer KM, Zal T, Adam L, Dinney CP, Drezek RA, West JL, Hafner JL. The stabilization and targeting of surfactant-synthesized gold nanorods. *Nanotechnology* 2009; 20: 434005.
- Pan D, Pramanik M, Senpan A, Yang X, Scott, MJ, Song KH, Gaffney PJ, Wickline SA, Wang LV, Lanza GM. Molecular photo acoustic imaging (PAI) with ligand-directed gold nanobeaccons. *Angew Chem Int Ed* 2009; 48: 4170–4173.
- Pan D, Pramanik M, Senpan A, Ghosh S, Wickline SA, Wang LV, Lanza GM. Near infrared photoacoustic detection of sentinel lymphnodes with gold nanobeaccons. *Biomaterials* 2010; 31: 4088–4093.
- Pan D, Pramanik M, Senpan A, Wickline SA, Wang LV, Lanza GM. A facile synthesis of novel self-assembled gold nanorods designed for near-infrared imaging. *J Nanosci Nanotechnol* 2010; 10: 8118–8123.
- Pan D, Pramanik M, Senpan A, Stacy A, Zhang H, Wickline SA, Wang LV, Lanza GM. Molecular photoacoustic imaging of angiogenesis with integrin targeted gold nanobeaccons. *FASEB J* 2011; 25: 875–882.
- Raut S, Gaffney PJ. *Thromb Haemostas* 1996; 76: 56–64.
- Song KH, Wang LHV. *J Biomed Opt* 2007; 12: 060503 (1–3).
- Pramanik M, Ku G, Li CH, Wang LHV. *Med Phys* 2008; 35: 2218–2223.
- Krag D, Weaver D, Ashikaga T, Moffat F, Klimberg VS, Shriver C, et al. The sentinel node in breast cancer – a multicenter validation study. *New Engl J Med* 1998; 339: 941–946.
- McMasters KM, Tuttle TM, Carlson DJ, Brown CM, Noyes RD, Glaser RL, et al. Sentinel lymph node biopsy for breast cancer: a suitable alternative to routine axillary dissection in multi-institutional practice when optimal technique is used. *J Clin Oncol* 2000; 18: 2560–2566.
- Chen SL, Iddings DM, Scheri RP, Bilchik AJ. Lymphatic mapping and sentinel node analysis. *CA Cancer J Clin* 2006; 56: 292–309.
- Laruelle G, Francios J, Billon L. Self-assembly in aqueous media of amphiphilic poly acrylic acid based di-block copolymers synthesized by direct nitroxide-mediated polymerization. *Macromol Rapid Commun* 2004; 25: 1839–1844.
- Huang HY, Kowalewski T, Remsen EE, Gertzmann R, Wooley KL. Hydrogel-coated glassy nanospheres: a novel method for the synthesis of shell cross-linked knedel. *J Am Chem Soc* 1997; 119: 11653–11659.
- Wu J, Eisenberg A. Proton diffusion across membranes of vesicles of poly(styrene-*b*-acrylic acid) diblock copolymers. *J Am Chem Soc* 2006; 128: 2880–2884.
- Xu J, Sun G, Rossin R, Hagooley A, Li Z, Fukukawa K, et al. Labeling of polymer nanostructures for medical imaging: importance of charge density, spacer length, and crosslinking extents. *Macromolecules* 2007; 40: 2971–2973.
- Zhang HF, Maslov K, Stoica G, Wang LHV. *Nat Biotechnol* 2006; 24: 848–851.
- Brooks PC, Clark RAF, Cheresch DA. Requirement of vascular integrin avb3 for angiogenesis. *Science* 1994; 264: 569–571.
- Winter P, Neubauer A, Caruthers S, Harris T, Robertson J, Williams T, Schmieder A, Hu G, Allen J, Lacy E, Wickline S, Lanza G. Endothelial alpha(nu)beta(3)-integrin targeted fumagillin nanoparticles inhibit angiogenesis in atherosclerosis. *Arterioscler Thromb Vasc Biol* 2006; 26: 2103–2109.
- Winter PM, Schmieder AH, Caruthers SD, Keene JL, Zhang H, Wickline SA, Lanza GM. Minute dosages of alpha(nu)beta3-targeted fumagillin nanoparticles impair Vx-2 tumor angiogenesis and development in rabbits. *FASEB J* 2008; 22: 2758–2767.
- Cheresch DA. Integrins in thrombosis, wound healing and cancer. *Biochem Soc Trans* 1991; 19: 835–838.
- Friedlander M, Theesfeld CL, Sugita M, Fruttiger M, Thomas MA, Chang S, Cheresch DA. Involvement of integrins an b3 and an b5 in ocular neovascular diseases. *Proc Natl Acad Sci USA* 1996; 93: 9764–9769.
- De Nichilo M, Burns G. Granulocytemacrophage and macrophage colonystimulating factors differentially regulate a v integrin expression on cultured human macrophages. *Proc Natl Acad Sci USA* 1993; 90: 2517–2521.
- Helluin O, Chan C, Vilaire G, Mousa S, DeGrado WF, Bennett JS. The activation state of avb 3 regulates platelet and lymphocyte adhesion to intact and thrombin-cleaved osteopontin. *J Biol Chem* 2000; 275: 18337–18343.
- Itoh H, Nelson P, Mureebe L, Horowitz A, Kent K. The role of integrins in saphenous vein vascular smooth muscle cell migration. *J Vasc Surg* 1997; 25: 1061–1069.

37. Carreiras F, Denoux Y, Staedel C, Lehman M, Sichel F, Gauduchon P. Expression and localization of  $\alpha_v$  integrins and their ligand vitronectin in normal ovarian epithelium and in ovarian carcinoma. *Gynecol Oncol* 1996; 62: 260–267.
38. Kageshita T, Hamby CV, Hirai S, Kimura T, Ono T, Ferrone S. Differential clinical significance of  $\alpha_v\beta_3$  expression in primary lesions of acral lentiginous melanoma and of other melanoma histotypes. *Int J Cancer* 2000; 89: 153–159.
39. Hu G, Lijowski M, Zhang H, et al. Imaging of Vx-2 rabbit tumors with  $\alpha_v\beta_3$ -integrin-targeted  $^{111}\text{In}$  nanoparticles. *Int J Cancer* 2007; 120: 1951–1957.
40. Wang XD, Pang YJ, Ku G, Xie XY, Stoica G, Wang LV. Noninvasive laser-induced photoacoustic tomography for structural and functional in vivo imaging of the brain. *Nat Biotechnol* 2003; 21: 803–806.
41. Siphanto RI, Thumma KK, Kolkman RG, van Leeuwen TG, de Mul FF, van Neck JW, van Adrichem LN, Steenbergen W. Serial noninvasive photoacoustic imaging of neovascularization in tumor angiogenesis. *Opt Express* 2005; 13: 89–95.
42. Maslov K, Zhang HF, Hu S, Wang LV. Optical-resolution photoacoustic microscopy for in vivo imaging of single capillaries. *Opt Lett* 2008; 33: 929–931.
43. Lao Y, Xing D, Yang S, Xiang L. Noninvasive photoacoustic imaging of the developing vasculature during early tumor growth. *Phys Med Biol* 2008; 53: 4203–4212.
44. Zhang EZ, Laufer JG, Pedley RB, Beard PC. In vivo high-resolution 3D photoacoustic imaging of superficial vascular anatomy. *Phys Med Biol* 2009; 54: 1035–1046.
45. Jose J, Manohar S, Kolkman RG, Steenbergen W, van Leeuwen TG. Imaging of tumor vasculature using Twente photoacoustic systems. *J Biophoton* 2009; 2: 701–717.
46. Hu S, Oladipupo S, Yao J, Santeford AC, Maslov K, Kovalski J, Arbeit JM, Wang LV. Optical-resolution photoacoustic microscopy of angiogenesis in a transgenic mouse model. *Proc SPIE* 2010; 7564: 756406.
47. Wang LV, Xie X, Oh JT, Li MN, Ku G, Ke S, Similache S, Li C, Stoica G. Combined photoacoustic and molecular fluorescence imaging in vivo. *IEEE Eng Med Biol Proc* 2005; 7: 190–192.
48. Xie X, Oh JT, Li ML, Ku G, Wang X, Ke S, Li C, Similache S, Stoica G, Wang LV. Photoacoustic tomography and molecular fluorescence imaging: dual modality imaging of small animal brains in vivo. *Proc SPIE* 2005; 5697: 107–110.
49. De la Zerde A, Zavaleta C, Keren S, Vaithilingam S, Bodapati S, Liu Z, Levi J, Smith BR, Ma TJ, Oralkan O, Cheng Z, Chen X, Dai H, Khuri-Yakub BT, Gambhir SS. Carbon nanotubes as photoacoustic molecular imaging agents in living mice. *Nat Nanotechnol* 2008; 3: 557–562.
50. Xie X, Li ML, Oh JT, Ku G, Wang W, Li C, Similache S, Lungu GF, Stoica G, Wang LV. Photoacoustic molecular imaging of small animals in vivo. *Proc SPIE* 2006; 6086: 608606.
51. Xiang L, Yuan Y, Xing D, Ou Z, Yang S, Zhou F. Photoacoustic molecular imaging with antibody-functionalized single-walled carbon nanotubes for early diagnosis of tumor. *J Biomed Opt* 2009; 14: 021008.
52. Weissleder R, Bogdanov A Jr, Tung CH, Weinmann HJ. Size optimization of synthetic graft copolymers for in vivo angiogenesis imaging. *Bioconjug Chem* 2001; 12: 213–219.
53. Harris TD, Rajopadhye M. Vitronectin receptor antagonist pharmaceuticals. Bristol-Myers Squibb Pharma Company. US patent 6,511,648.
54. Meoli DF, Sadeghi MM, Krassilnikova S, Bourke BN, Giordano FJ, Dione DP, Su H, Edwards DS, Liu S, Harris TD, Madri JA, Zaret BL, Sinusas AJ. Noninvasive imaging of myocardial angiogenesis following experimental myocardial infarction. *J Clin Invest* 2004; 113: 1684–1691.
55. Miyauchi A, Alvarez J, Greenfield EM, Teti A, Grano M, Colucci S, Zamboni-Zallone A, Ross FP, Teitelbaum SL, Cheres D, et al. Recognition of osteopontin and related peptides by an  $\alpha_v\beta_3$  integrin stimulates immediate cell signals in osteoclasts. *J Biol Chem* 1991; 266: 20369–20374.